Self-focusing of a spatially modulated beam within the paraxial complex geometrical optics framework in low-density plasmas

A Ruocco, G Duchateau and V T Tikhonchuk

Published version information

Citation: A Ruocco, G Duchateau and VT Tikhonchuk. Self-focusing of a spatially modulated beam within the paraxial complex geometrical optics framework in low-density plasmas. Plasma Phys Contr F 63 (2021): 125019

DOI: 10.1088/1361-6587/ac2e43

Self-focusing of a spatially modulated beam within the Paraxial Complex Geometrical Optics framework in low-density plasmas

A. Ruocco,[1,2,a] G. Duchateau,[2,3] and V. T. Tikhonchuk[2,4]
[1] *Central Laser Facility, STFC Rutherford Appleton Laboratory, Harwell Oxford, Didcot, Oxford OX11 0QX, United Kingdom*
[2] *Centre Lasers Intenses et Applications (CELIA) UMR 5107, Université de Bordeaux, CNRS, CEA, 33405 Talence, France*
[3] *CEA, CESTA, 15 Avenue des Sablieres, CS60001, 33116 Le Barp Cedex, France*
[4] *ELI-Beamlines, Institute of Physics, Czech Academy of Sciences, 25241 Dolní Břežany, Czech Republic*

Accurate modelling of ponderomotive laser self-focusing may represent a key for the success of inertial confinement fusion, especially within the shock ignition approach. From a numerical point of view, implementation of a paraxial complex geometrical optics (PCGO) method has improved the performance of the hydrodynamics code CHIC, but i) overestimating ponderomotive speckle self-focusing in reduced two-dimensional geometry, and ii) not accounting for speckle intensity statistics. The first issue was addressed in our previous work [A. Ruocco *et al.*, Plasma Phys. Control. Fusion **61** 115009 (2019)]. Based on those results, here we propose a novel PCGO scheme for modelling spatially modulated laser beams by i) creating Gaussian speckles, and ii) emulating the realistic speckle intensity statistics. Self-focusing of spatially modulated beams in a homogeneous stationary plasma with this method is studied. This investigation evidences that plasma smoothing does not reduce the speckle intensity enhancement at long time scales when the average beam intensity is twice above the speckle critical intensity. Comparison against electromagnetic simulations confirms that this approach improves the description of self-focusing of high-intensity speckles within the PCGO model.

Keywords: laser-plasma interaction, hydrodynamics codes, ponderomotive force, inertial confinement fusion, optical smoothing, geometrical optics

I. INTRODUCTION

In inertial confinement fusion[1,2] (ICF), nanosecond, high-energy laser beams are used to compress a multi-layer capsule to trigger nuclear reactions of the Deuterium-Tritium gas to obtain a net energy gain. In the direct-drive approach, high-intensity lasers directly irradiate the capsule, leading to its implosion. The laser intensities are such that the thresholds of nonlinear laser-plasma coupling such as ponderomotive laser self-focusing and parametric instabilities can be overcome. These processes may break the symmetry of target illumination, reducing the capsule implosion uniformity. Nonlinear phenomena are of a high concern in spike pulse-plasma interaction within the direct-drive shock ignition (SI) approach[3,4]. In SI, a low intensity pulse drives a slow implosion, whereas a spike pulse launches an inward-propagating strong shock wave that triggers the ignition of the capsule core. Despite SI promises ignition at a lower laser energy than conventional hot-spot schemes[5–7], it presents some intrinsics issues related to hot electron production due to nonlinear laser-plasma interaction during the intense spike pulse[5,8–10].

To mitigate nonlinear phenomena and improve the laser-target coupling, optical smoothing techniques are employed in ICF experiments. Phase plates placed after the beam focusing lens break the spatial coherence of the incident beam and create in the far-field small-scale spatial modulations, known as speckle pattern[11–13]. The speckles intensity follows a statistical distribution.[14,15] Although it has been demonstrated that under certain conditions, spatial smoothing improves the quality of laser-plasma coupling[16], nonlinear phenomena may still occur in the high-intensity tail of this distribution, even though the average laser intensity is below the nonlinear processes threshold[17–19].

Nonlinear effects and more sophisticate laser modelling must be included in radiation-hydrodynamics codes in order to enhance their performances. Laser propagation and energy deposition are often modelled in a simplified way by using ray-tracing (RT) techniques[20]. In this approach, laser beam is split in several rays each of them carrying a fraction of the total power and depositing it in plasma according the law of collisional absorption. However, ray tracing cannot account for: i) speckled laser beams, ii) collisionless laser energy absorption and iii) nonlinear laser-plasma coupling processes. In order to include these aspects, advanced methods of geometrical optics have been developed with applications in the domains of magnetic[21–24] and inertial confinement fusion[25–27] .These methods provide the possibility for evaluation of the wave amplitude along the ray trajectory, but they require significant computation resources and do not properly model smoothed beam intensity distributions. In this work, we concentrate on the module implemented in the radiation-hydrodynamics code CHIC[28], relying on the paraxial complex geometrical optics (PCGO) equations[29] in two-dimensional (2D) planar geometry[27].

[a] Electronic mail: alessandro.ruocco@stfc.ac.uk

The beamlet represents the basic element of the PCGO description: it stands for a ray with a defined width and Gaussian-like intensity profile, whose centroid obeys the standard geometrical optics laws. This approach has opened the possibilities for modelling of nonlinear laser-plasma coupling and implementation of optical smoothing techniques[30]. In case of spatial smoothing, laser intensity fluctuations are produced by randomly distributing the focal spots of several beamlets in the focal volume. Combination of beamlets allows to create the speckle pattern in the far-field. To be computationally efficient and compatible with the hydrodynamics spatial resolution, the beamlets phases are not evaluated when they overlap and give rise to a speckle. For this reason, a PCGO speckle is several times larger than a real speckle. On the other hand, the total beam intensity is preserved in order to correctly reproduce large scale intensity-dependent laser-target interaction processes such as target ablation, target compression and hot-electron production. Moreover, randomly-propagating beamlets generate speckles of uncontrolled shape, further inducing an error in the development of ponderomotive effects compared to the real Gaussian speckle pattern. Then, whereas the total beam intensity in PCGO coincides with the real beam intensity, the probability distribution of the speckle intensities does not have the expected shape[14,15]. As a consequence of these considerations, speckle ponderomotive self-focusing may be incorrectly described.

To properly account for ponderomotive self-focusing in the hydrodynamics codes along with laser speckle pattern, it is then necessary to develop a method which i) permits to have a better control of speckle shape and its self-focusing process and ii) include the correct speckle intensity statistics. The first objective has been already accomplished in our previous work[31], where a single PCGO speckle was created by superposing three PCGO beamlets whose positions and intensities are chosen such that the speckle has a given Gaussian intensity profile.

In the present work, we extend the single speckle method[31] to a multi-speckle case, where each speckle exhibits a Gaussian profile obtained by overlapping three beamlets. Furthermore, the speckle pattern is built such that the distribution of the speckles intensities follow an exponential-like law such as $\exp\left(-I_s/\langle I\rangle\right)$, where I_s and $\langle I\rangle$ are the speckle and average beam intensity, respectively. Such a method is referred to as *semi-deterministic algorithm*, in contrast to the standard PCGO method in the following referred to as *random algorithm*. We show here that the semi-deterministic approach improves the description of laser-plasma coupling in regimes where ponderomotive effects develop. Our new method shows a good agreement with simulations performed with an electromagnetic code for similar laser and plasma conditions[32], especially for the high-intensity tail of the speckle distribution.

The paper is organized as follows: guiding theoretical considerations on self-focusing in paraxial approximation, description of PCGO-based algorithms and our previous results on self-focusing of a single PCGO speckle are presented in Sec. II. In Sec. III, we introduce the new semi-deterministic algorithm for speckle patterns in PCGO-CHIC formalism. Study of self-focusing of the spatially modulated beam within the semi-deterministic algorithm is illustrated in Sec. IV. A comparison to previous results and to the random algorithm is discussed in Sec. V. The summary of our results is given in Sec. VI.

II. PONDEROMOTIVE SELF-FOCUSING AND DESCRIPTION OF PCGO-BASED ALGORITHMS

A. Ponderomotive beam self-focusing in paraxial approximation

In the paraxial approximation, the following set of equations governs the laser-plasma coupling[33] :

$$\left[\frac{\partial}{\partial t}+v_g\frac{\partial}{\partial x}-i\frac{c^2}{2\omega_0}\nabla_\perp^2-i\frac{\omega_0}{2}\frac{\delta n}{n_c}\right]\mathbf{E}=0. \tag{1}$$

$$\frac{\partial n_e}{\partial t}+\nabla\left(n_e\mathbf{v}_p\right)=0 \tag{2}$$

$$n_e\left[\frac{\partial}{\partial t}+\left(\mathbf{v}_p\cdot\nabla\right)\right]\mathbf{v}_p=-\nabla P_T-\nabla U_p \tag{3}$$

The first equation describes the spatiotemporal evolution of the laser electric field $\mathbf{E}$. The second and third equations describe the plasma dynamics within the fluid theory: the equations represent the continuity equation and the fluid equation of motion, respectively. Here n_e is the electron density, whereas $\mathbf{v}_p$ is the fluid velocity of the plasma. The coordinate x corresponds to the direction of laser beam propagation, $\delta n = n_e - n_{e0}$ is the electron density perturbation with respect to the initial electron density n_{e0}, $n_c = m_e\epsilon_0\omega_0^2/e^2$ is the plasma critical density, c and ω_0 are the speed of light in vacuum and the laser frequency, respectively, ϵ_0 is the vacuum dielectric permittivity, e and m_e are the elementary charge and electron mass, $v_g = c\sqrt{1-n_e/n_c}$ is the light group velocity in the plasma. In Eq. (1), $\nabla_\perp^2 = \partial_y^2+\partial_z^2$ is the transverse Laplacian in Cartesian coordinates, which accounts for the beam diffraction, whereas the fourth term is responsible for beam refraction on self-induced density perturbation. In Eq. (3), $U_p = n_e e^2|E_0|^2/4m_e\omega_0^2 = n_e/(2cn_c)I_0$ is the ponderomotive pressure, $I_0 = v_g\epsilon_0|E_0|^2/2$ being the laser intensity, and $P_T = n_i(ZT_e+\gamma T_i)$ is the thermal plasma pressure, where $n_i = n_e/Z$ is the ion density in the quasi-neutral approximation, and Z is the ion charge. Here γ represents the heat capacity ratio. All along this work, we take $\gamma = 3$, which corresponds to one degree of freedom as ion motion is transverse to the laser propagation direction. The last terms in Eqs. (1) and (3) link the

electric field variation to the plasma density perturbation driven by the the ponderomotive force $\mathbf{F}_p = -\nabla U_p$.

Ponderomotive self-focusing affects the beam propagation when the beam power, or equivalently the beam intensity, overcomes a critical value. The beam power is a geometry-dependent quantity, whereas the intensity is geometry-independent. Considering a beam of a Gaussian profile, the critical intensity reads[34–36]

$$I_{0c} = 1.8 \times 8 \frac{n_c(T_e + 3T_i/Z)c^2 v_g}{\omega_{pe}^2 w_b^2}, \tag{4}$$

where $\omega_{pe}^2 = e^2 n_e/(m_e \epsilon_0)$ is the electron plasma frequency and w_b is the beam width. The critical power in different geometries can be recovered from Eq. (4). In case of Gaussian beams of cylindrical geometry, the beam critical power reads $P_c^{3D} = (\pi/2) w_b^2 I_{0c}$. Considering that the critical intensity I_{0c} goes as $\sim 1/w_b^2$, the critical power in this geometry does not depend on the beam waist. In two-dimensional planar geometry, such as in PCGO-CHIC, the power of a Gaussian beam reads $P_c^{2D} = \sqrt{\pi/2} h w_b I_{0c}$, where h is the unity length in the artificial third dimension added to preserve energy definition in 2D. Unlike in cylindrical geometry, the critical power P_c^{2D} in 2D planar geometry goes as $\sim 1/w_b$. Then, 2D larger PCGO speckles are more prone to ponderomotively self-focus. In our previous work, we have compensated this overestimation of self-focusing effects by building speckles whose critical power is twice larger than the critical power of a Gaussian beam (see Sec. II C 2).

B. Spatially modulated beams and related plasma-induced incoherence

In ICF beamlines, the speckle pattern in the far-field is generated by a phase plate, which breaks the beam spatial coherence as each element of the plate induces a random phase variation to different parts of the beam. The size and the number of speckles are related to the laser wavelength and the focal length: in vacuum, the transverse size of spatial modulations is[14,15]

$$w_s = \frac{2f\lambda}{\pi D}, \tag{5}$$

where $\lambda = 2\pi c/\omega_0$ is the laser wavelength, f is the focal length and D is the lens diameter; the longitudinal size of a speckle is

$$x_s = \frac{\pi w_s^2}{\lambda} \tag{6}$$

Defining N_s as the number of speckles in the far-field, geometrical and optical considerations[14] estimate that $N_s \simeq (D/L)^3$, where L is the characteristic size of the phase plate element. N_s is typically of the order of 10^3-10^4. It is then convenient to characterize the speckles intensity by using a statistical approach: the number of speckles of intensity I_s with respect to the average beam intensity $\langle I \rangle$ is represented by[14,15]:

$$M(I_s) = f\left(I_s/\langle I \rangle\right) \exp\left(-\frac{I_s}{\langle I \rangle}\right), \tag{7}$$

where $f\left(I_s/\langle I \rangle\right)$ is a slowly varying function. This shape is typical of a pattern where speckles have a Gaussian form. The high-intensity speckles may be a source of nonlinear laser-plasma coupling.

The inter-speckle coupling gives rise to the plasma-induced smoothing: this phenomenon consists in a reduction of the degree of spatial and temporal coherence of the beam due to beam scattering on small-scale laser-driven density fluctuations[32,37–39]. A signature of this process is angular and spectral broadening of the forward scattered light. Plasma-induced incoherence is caused by interference of plasma waves produced inside a self-focused speckle with fluid plasma waves excited in other speckles. Depending on the speckle-plasma dynamics and on the laser intensity, these multiple interactions may lead to a stabilization of speckle self-focusing, or to a modification of the speckle statistics. In Sec. IV C we study plasma smoothing by means of PCGO-CHIC simulations.

C. CHIC code and PCGO methods

CHIC is a radiation-hydrodynamics code solving the single fluid equations (2) and (3) on a Lagrangian or arbitrary Lagrangian-Eulerian mesh. The model includes also two equations accounting for energy conservation of both electron and ion species[28]. In its standard version, laser beam propagation and energy deposition are modeled by ray-tracing. To improve laser-plasma coupling, a method based on the paraxial complex geometrical optics (PCGO)[29] has been implemented in two-dimensional (2D) planar geometry: such a model is referred to as the *thick-ray* model[27]. In this approach, a ray is represented by a beamlet with a Gaussian intensity profile $I_b(\tau, q)$ given by

$$I_b(\tau, q) = I_0(\tau) e^{-2\frac{q^2}{w_b^2}}, \tag{8}$$

where τ is the ray curvilinear coordinate, q is the transverse coordinate normal to τ, $w_b = w_b(\tau)$ is the beamlet spatial width, $I_0(\tau) = w_0 I_0/w_b(\tau)$ is the beamlet intensity on the centroid, and w_0 and I_0 are the initial beamlet waist and the initial peak intensity, respectively. The beamlet trajectory $\mathbf{r}_b = \mathbf{r}_b(\tau)$ obeys the ray equation

$$\frac{d^2 \mathbf{r}_b}{d\tau^2} = \frac{c^2}{2} \nabla N^2, \tag{9}$$

where $N^2 = 1 - n_e/n_c$ is the local refractive index of the plasma. The beamlet waist w_b is related to the complex

wavefront curvature B: $w_b(\tau) = \sqrt{2\omega_0/(c\,\mathrm{Im}B)}$. The wavefront curvature B is found along the ray trajectory according to an ordinary Riccati-type differential equation:

$$\frac{1}{c}\frac{dB}{d\tau} + B^2 = -\frac{3}{4\mathrm{Re}\epsilon_c}\left(\frac{\partial \mathrm{Re}\epsilon_c}{\partial q}\right)^2 + \frac{1}{2}\frac{\partial^2 \mathrm{Re}\epsilon_c}{\partial q^2}, \quad (10)$$

where ϵ_c is the complex permittivity of the plasma around the beamlet centroid. By solving Eqs. (9) and (10), one finds the beamlet intensity as in Eq. (8). The beamlet intensity is then projected onto the hydrodynamics grid. In Cartesian coordinates. The ponderomotive force is calculated as an external force acting on plasma through the term $\mathbf{F}_p = -\nabla U_p$ in Eq. (3).

1. Spatially modulated beams in PCGO-CHIC: the random method

The thick-ray method has provided the possibility to create beams with spatial modulations via overlapping several beamlets[40]. When the code calculates the beamlets intensity envelope, the phase variation along the beamlet trajectory is not considered and beamlets are propagated from the simulation boundaries to the far-field in three steps. The first step concerns the definition of the initial beam characteristics: the beam width in the far-field w_B, the beam power P_B, the order of the super-Gaussian profile n and the beam focal position (x_B, y_B). The average beam intensity $\langle I\rangle$ is *a posteriori* computed through the relation

$$\langle I\rangle = \frac{P_B}{h\int_{-l_y}^{l_y} e^{-2\left|\frac{y}{w_B}\right|^n} dy}, \quad (11)$$

where l_y is a length few times larger than w_B. The second step, beam-splitting, consists in the division of the laser beam into N_b beamlets of equal width w_b at the beam entry boundary such as the intensity beamlets envelope reproduces the incident laser beam profile at the near-field. The final stage consists in propagating the beamlets from their origin to their focal spot positions, which are randomly chosen inside a focusing box in the far-field. The dimension of the focusing box is related to the longitudinal speckle size x_s, defined by Eq. (6), the speckle waist w_s, defined by Eq. (5), and the total beam width w_B. Each PCGO beamlet propagates according to Eq. (9), and with an intensity profile defined by Eq.(8). Thus, the local laser intensity in plasma $I(x,y)$ is calculated as a sum of N_b neighbor beamlets intensities $I_{bj}(\tau_j(x,y), q_j(x,y))$[27,40]:

$$I(x,y) = \sum_{j=1}^{N_b} I_{bj}(\tau_j(x,y), q_j(x,y)), \quad (12)$$

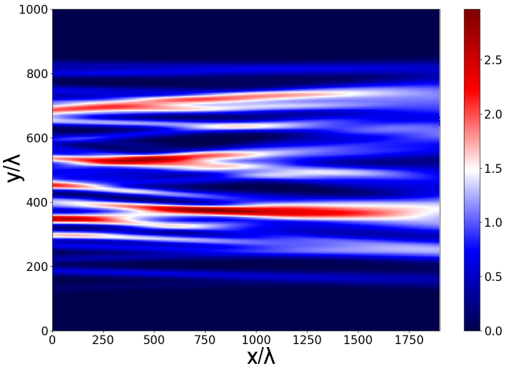

FIG. 1: Laser intensity in the far-field normalized to the average intensity realized with the random algorithm. The laser comes from the left side. The spatial coordinates are in laser wavelength units.

where $(x(\tau_j), y(\tau_j))$ is ray coordinate corresponding to the closest distance between the trajectory of the beamlets and the observation point (x,y): only a limited number of beamlets passing at a distance of the order of the beamlet width contribute to the local intensity. Local intensity maxima are formed where two or more beamlets cross each others, representing then the speckles. To save computational time, the beamlet interference is neglected in the local laser intensity calculation. This gives rise to larger speckles, whose individual self-focusing has been already studied[31]. The ponderomotive pressure in plasma is evaluated as sum of the ponderomotive pressures locally induced by the beamlets.

Figure 1 shows the result of one realization by employing the random algorithm: the color bar corresponds to the initial laser intensity distribution normalized to the average intensity $\langle I\rangle$ in the far-field. The beam focal position is located at $(500\lambda, 500\lambda)$. The red zones represent local intensity maxima, i.e. the speckle pattern. The speckles present an irregular intensity profile created according to Eq. (12), which is a consequence of the beamlets' random inclination and random choice of beamlets' focal positions. For each realization, the speckle intensity distribution does not reproduce the distribution given by Eq. (7) as it is not included in the algorithm. The exponential-like form of the speckle intensity distribution can be realized by repeating the same simulation several times: for example, to obtain the speckle intensity statistics for 1000 speckles, one may perform 50 runs when considering a number of PCGO speckles equal to 20 for each run. Such method of speckle initialization limits the applicability of PCGO for investigating the ponderomotive effects in a spatially modulated beam because the speckle intensity statistics cannot be controlled in a single realization.

In Sec. III, we present the PCGO method developed to create a spatially modulated beam of Gaussian-like

speckles where the distribution function Eq. (7) is included. From Sec. IV then, we study the interaction of high-intensity speckles with the plasma when ponderomotive self-focusing operates, a feature independent of the overall beam shape.

2. Self-focusing of a PCGO speckle: modification of the critical intensity

In this paragraph, we recall the main result obtained in our previous work[31]. Since its conception[30], the PCGO-based method has been developed to preserve the laser intensity, but considering speckles several times larger than real speckles. As it follows from Sec. II A, the critical power in 2D geometry depends on the transverse size of the speckle. For this reason, PCGO large speckles can be more prone to ponderomotive effects compared to real ones. This characteristics stands for an undesired downsize of PCGO description of nonlinear laser-plasma processes. Then, one PCGO beamlet cannot represent a single real speckle. As demonstrated in our work[31], ponderomotive effects are reduced when three beamlets are overlapped in such a way that their intensity envelope creates a desired Gaussian intensity profile[31]. A parameter measuring this behaviour is the aspect ratio $x_s\lambda/(w_b^2\pi)$, where w_b is the instantaneous beam width minimum, whereas x_s is the speckle Rayleigh length, i.e. the longitudinal distance from the speckle intensity maximum to the position where the intensity decreases by a factor of $\sqrt{2}$. For Gaussian beamlets, this aspect ratio is preserved during the beamlet dynamics and is equal to 1. Instead, we have found that in three-beamlet speckles, the aspect ratio changes in time and its time average is twice larger than the aspect ratio of a single beamlet. Comparing aspect ratios for different intensities and the related peak intensity dynamics, we observed that the three-beamlet speckle acts as a Gaussian beamlet of a half of power. This consideration has lead us to a new definition of the critical intensity for the three-beamlet speckle I_{0c}^{3b} when compared to a single Gaussian beamlet of similar shape:

$$I_{0c}^{3b} = 2I_{0c}, \tag{13}$$

where the factor of 2 is related to the increased aspect ratio in a three-beamlet speckle when it self-focuses. In the following, we extend this approach to spatially modulated beams.

III. THE SEMI-DETERMINISTIC SPECKLE PATTERN

The semi-deterministic method allows to control the speckle intensity distribution, which is crucial for including self-focusing effects in PCGO-CHIC simulations. The algorithm is based on our previous results recalled in Sec. II C 2, and it has been developed by starting from two

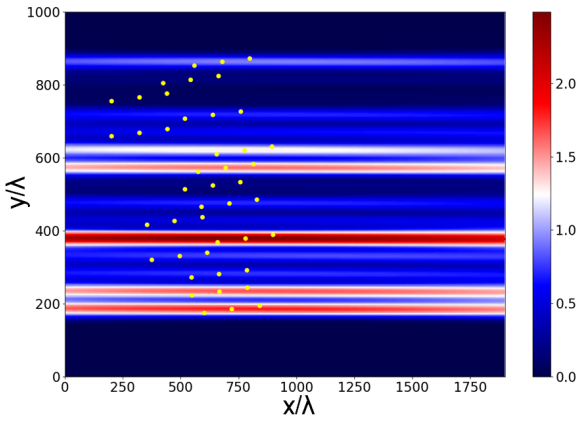

FIG. 2: Semi-deterministic speckle pattern: laser intensity normalized to the average intensity in the far-field. The yellow points stand for the beamlet focal positions. The laser comes from the left side. The spatial coordinates are in laser wavelength units.

principles: i) every speckle is composed of three beamlets, creating a Gaussian intensity profile, and ii) the probability distribution of the speckle statistics follows an exponential law Eq. (7) with $f\left(I_s/\langle I\rangle\right) = \text{const}$. Other distribution functions can be explored by varying $f\left(I_s/\langle I\rangle\right)$.

The algorithm operates as follows: once defined the speckle width w_s and the beam width w_B, the number of speckles N_s is computed:

$$N_s = \frac{w_B}{w_s}. \tag{14}$$

This allows to cover the beam area in the far-field with N_s speckles, whose area is $4w_s x_s$. In order to be compatible with the the hydrodynamics grid, the speckle width has to be in the range $w_s = 15\lambda - 60\lambda$, depending on the laser wavelength. That sets an upper limit to the number of speckles, which spans between 15 and 50. At the second step, the algorithm confers to each speckle a random intensity value within a range such that the ensemble of speckle intensities obeys Eq. (7). Despite the number of speckles created within the PCGO algorithm is smaller than the number of real speckles, the speckle intensity distribution covers the range $[0.1,4]\langle I\rangle$, which is representative of a real speckle intensity distribution[15].

By spatially varying the beamlet configuration, different spatial speckle patterns can be explored: for instance, patterns where inter-speckle distance is randomly varied, or speckles with arbitrary inclinations with respect to the laser beam axis. In the design used throughout this paper, the beamlets are initialized to form parallel speckles with a constant transverse distance between them: considering that the beam focal positions is located at (x_B, y_B), the transverse coordinate y_s^j of the jth speckle is:

$$y_s^j = y_B + (N_s - 2j) y_w w_s, \tag{15}$$

where y_w is a numerical factor permitting to increase or decrease the focusing box area. The longitudinal spot coordinate x_s^j of the jth speckle is randomly chosen in the interval $[x_B - x_s; x_B + x_s]$. At the third step, the speckle-splitting process is introduced: around each speckle focal position, three beamlets are initialized by starting with their focal positions. These beamlets are located such that the central one has the same coordinates as the relative speckle, whereas the two outer beamlets are shifted to $(x_s^j \pm 0.15x_s, y_s^j \pm w_s/2)$, respectively[31]. The beamlets have the same width, equal to the speckles width. Only one degree of freedom on the longitudinal beamlets focal positions is considered in this version of semi-deterministic method. This could be eventually extended to two spatial degrees of freedom, longitudinal and transverse. At the next step, the speckle intensity I_s is equally divided over the three beamlets, thus $I_b = I_s/3$. Similarly to the random method, the last step consists in the evaluation of the beamlet characteristics at the simulation boundary, from which the beamlets are injected in the simulation region. At the end of the initialization, the beam presents small-scale modulations in form of Gaussian-like three-beamlet speckles, each of them having a Gaussian transverse and longitudinal intensity profile[31]. This semi-deterministic beamlets distribution produces the speckle pattern as displayed in Fig. 2: here the color bar represents the beam intensity normalized to the average beam intensity $\langle I \rangle$. The speckle pattern is clearly recognizable: each speckle consists of three-regularly focused beamlets with prescribed focusing spots (yellow dots) parallel to the beam axis. This regular pattern is due to the appropriate choice of beamlets' inclination and focal position. The speckle intensity profile is then created according to Eq. (12). The beam parameters are similar to the ones in Fig. 1: the beam focal position is $(500\lambda, 500\lambda)$, and its width is $w_B \approx 350\lambda$. Despite having the same parameters, it is evident that the semi-deterministic routine allows to create a more regular speckle pattern where all the parallel speckles have the same shape, i.e. same waist and longitudinal length, unlike the random algorithm speckle pattern, where the random choice of beamlets' angle of incidence and focal position create speckles of different shape and with arbitrary inclination. As a consequence, random speckles are usually shorter than semi-deterministic speckles.

It is interesting to compare other features of spatially modulated beams produced by the random and semi-deterministic algorithm: Fig. 3 shows the speckle abundance M, normalized such that $\int M(u)du = N_s$, where $u = I_s/\langle I \rangle$, as a function of speckle intensity normalized to the average beam intensity. The dashed blue line refers to the exponential speckle abundance described by Eq. (7) with $f(I_s/\langle I \rangle) = \text{const}$, the solid red line refers to one run realized with the semi-deterministic approach, the green lines refer to two different realizations by using the random algorithm. Since the semi-deterministic method is principally built by assigning a certain intensity to the speckles such that their intensities obey Eq. (7), the speckle abundance reproduces quite well the analytic formula. Instead, two different realizations with the random algorithm correspond to two different intensity abundances: the speckle statistics varies in each run and significantly departs from the exponential shape.

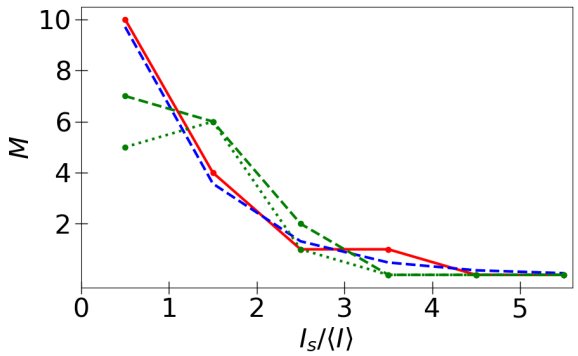

FIG. 3: Initial speckles abundance M: analytic formula (blue dashed line), one realization with semi-deterministic pattern for a single realization (red line) and two realizations with a random pattern (dashed and dotted green line). The abundance M is defined such that $\int M(g)dg = N_s$, where $g = (I_s/\langle I \rangle)$. Here, $N_s = 15$.

IV. SELF-FOCUSING OF A SEMI-DETERMINISTIC SPATIALLY MODULATED BEAM

In this section, we present the results of self-focusing of a spatially modulated beam generated with the semi-deterministic algorithm. The beam propagates into a homogeneous CH plasma ($Z = 3.5$) with density $n_{e0}/n_c = 0.1$ and temperature $T_e = 3T_i = 1$ keV. We have found in test studies (not shown here) that speckle self-focusing takes place in a zone near and beyond the focal point over a length shorter than the Raleigh length $x_s = 1200\lambda$. Consequently, for the studies presented in this paper we have chosen the plasma size of 1500λ and put the beamlet's focal point at the distance of 300-750λ from the entrance. The transverse dimension is 1000λ, which is about three times larger than the beam width: $w_B = 350\lambda$. The speckle pattern is shown in Fig. 2: the speckle width is $w_s \approx 20\lambda$, and it is equal to beamlets waist w_b^j. The beam is composed by 15 equidistant speckles, whose distance is larger than w_s, as displayed in the figure. With these parameters, the Gaussian beam critical intensity from Eq. (4) is $I_{0c} = 5.2 \times 10^{14}$ W/cm^2 for the laser wavelength of 0.35 μm. The red line in Fig. 3 represents the speckles intensity abundance for all the cases considered. The plasma conditions and speckles size are comparable to our previous work[31].

The speckle pattern behavior is explored by consider-

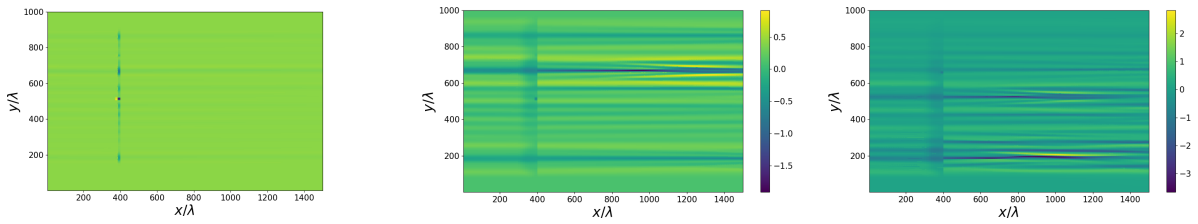

(a) (b) (c)

FIG. 4: Plasma perturbation $\delta n/n_{e0}$ for $\langle I\rangle/I_{0c} = 1.7$ as a function of the normalized spatial coordinates for (a) $t = 100$ ps and (b) $t = 210$ ps and c) for $\langle I\rangle/I_{0c} = 4$ at $t = 210$ ps. The color bar stands for the amplitude of the density perturbation $\delta n/n_{e0}$ (%). The spatial coordinates are in units of the laser wavelength λ. The laser enters from the left side.

ing different average laser intensities. We have performed 6 simulations lasting $t_f = 550$ ps, which is several times longer than the traveling time of a plasma perturbation through a speckle. The goal is to investigate individual speckle self-focusing at short time-scales along with inter-speckle interaction due to interference of plasma waves for long time-scales. Table I shows the list of the average beam intensities $\langle I\rangle$ considered normalized to the critical intensity I_{0c}: the first column refers to the average beam intensity, the second column refers to the intensity of the most intense speckle and the third column refers to the intensity of the less intense speckle. These cases range from the one where only one speckle has an intensity able to trigger self-focusing effects, i.e. $\langle I\rangle/I_{0c} = 0.4$ to the one where more than 80% of the speckles have an intensity at least equal to the critical intensity, as for the case $\langle I\rangle/I_{0c} = 5$. In Sec. IV A we study how the plasma perturbation forms inside the speckle area, in Secs. IV B-IV C we consider speckles self-focusing at short and long time scales, respectively. Section IV D is dedicated to the study of the variation of the speckle intensity abundance.

$\langle I\rangle/I_{0c}$	I_s^{max}/I_{0c}	I_s^{min}/I_{0c}
0.4	1	0.032
1	2.4	0.14
1.7	4.2	0.2
2.5	6	0.3
4	10	1
5	12	1.3

TABLE I: Average laser intensities for PCGO-CHIC simulations with semi-deterministic approach. First column: laser beam average intensity considered in the simulations. Second column: intensity of the most intense speckle. Third column: intensity of the less intense speckle. All the intensities are normalized to the critical intensity.

A. Plasma dynamics

In this section, we analyze the plasma response induced by a regular speckle pattern. Figure 4 shows the plasma perturbation $\delta n/n_{e0}$ for $\langle I\rangle/I_{0c} = 1.7$ as a function of the normalized spatial coordinates for (a) $t = 100$ ps and (b) $t = 280$ ps. The color bar stands for the amplitude of the density perturbation $\delta n/n_{e0}$ (%). The evolution of the density perturbation shows how the plasma waves generated inside the speckles transversely propagate outside of it: Fig.4(a) refers to a time when the plasma waves have not left yet the speckles, whereas Fig.4(b) displays the effect of plasma waves interference, which occurs when the plasma waves cover a distance that corresponds to time $2w_s/c_s \sim 180$ ps. We notice that this time-scale is related to the particular choice of constant inter-speckle distance. A different or a variable inter-speckle distance is expected to affect only the time-history of the dynamics, but not the overall long-time behavior.

Reduction of the maximum amplitude when comparing Fig. 4(b) to Fig. 4(a) is due to decrease of ponderomotive effects induced by plasma smoothing. By analyzing the evolution of plasma response with time and laser intensity, we find out that density perturbations with amplitude above 1% lead to strong modification of the intensity distribution in plasma, which occurs for $\langle I\rangle/I_{0c} > 1$. For these cases, the plasma density appears strongly modified, as shown in Fig. 4(c) for $\langle I\rangle/I_{0c} = 4$ at $t = 210$ ps. Behind the main self-focusing area placed at $x > 1250\lambda$, the density channels are distorted. This behavior is due to two phenomena: firstly, the amplitude of plasma perturbation is sufficiently large to create high-amplitude density variation, inducing a strong plasma modification even in low-intensity speckles which self-focus. As a side effect, a larger amount of speckles is deformed, losing their Gaussian shape because beamlets significantly deviate from their initial direction of propagation due to refraction in deep density channels. Both effects are analyzed in more details in the forthcoming sections.

Figure 5(a) displays the spatial Fourier transform of the density perturbation $\delta n/n_{e0}$ as a function of the transverse coordinate at $x = 1700\lambda$ and $t = 75$ ps for:

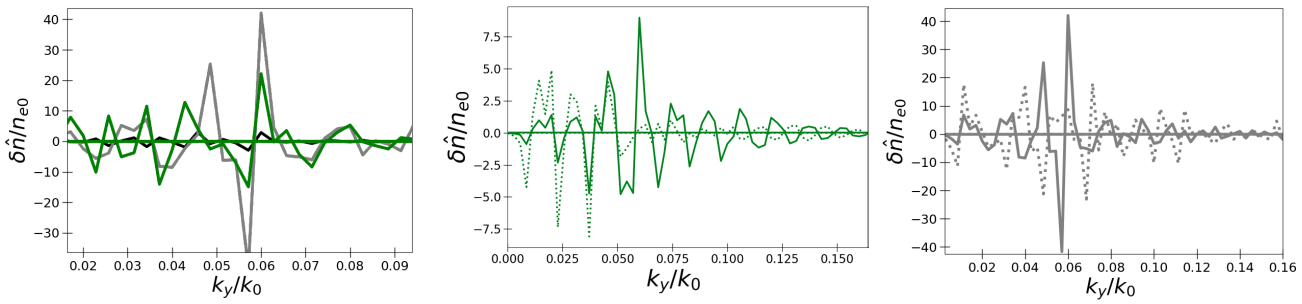

FIG. 5: Spatial Fourier transform of the transverse line-outs of density perturbation $\delta n/n_{e0}$ at $x = 1700\lambda$: a) $\langle I\rangle/I_{0c} = 0.4$ (black curve), $\langle I\rangle/I_{0c} = 1.7$ (green curve) and $\langle I\rangle/I_{0c} = 4$ (gray curve) at t = 75 ps; b) for $\langle I\rangle/I_{0c} = 1.7$ at t = 150 ps (solid green curve) and 300 ps (dotted green line); c) for $\langle I\rangle/I_{0c} = 4$ at t = 150 ps (solid gray curve) and 300 ps (dotted gray line). In all panels, the wave vectors k_y are normalized to the laser wave vector $k_0 = \omega_0/c$

$\langle I\rangle/I_{0c} = 0.4$ (black curve), $\langle I\rangle/I_{0c} = 1.7$ (green curve) and $\langle I\rangle/I_{0c} = 4$ (gray curve). As expected, the maximum of density amplitude occurs around $k_y \sim 0.06k_0$, which corresponds to the speckle width $w_s \sim 20\lambda$. The amplitude of these modes increases with the laser intensity, as more speckles undergo self-focusing. Other modes with different wave vectors k_y are produced since self-focusing may induce density variation at smaller and larger spatial scale, especially at larger laser intensities: the wave vector cut-off moves towards larger $|k_y|$ when increasing the laser intensity. Furthermore, the larger and shorter modes can be enhanced by nonlinear interaction of plasma waves.

Figures 5(b) and 5(c) show evolution of density perturbation spectrum for $t = 150$ ps (solid lines) and $t = 300$ ps (dotted lines) for $\langle I\rangle/I_{0c} = 1.7$ (green curves) and $\langle I\rangle/I_{0c} = 4$, respectively. The time $t = 150$ ps refers to independent speckle self-focusing, i.e. when plasma waves interference has not occurred yet, whereas at $t = 300$ ps, the plasma waves have already propagated a distance larger than inter-speckle distance. As a consequence, plasma waves interference and mode mixing can affect the speckles dynamics at long temporal scales. For the case $\langle I\rangle/I_{0c} = 1.7$, the density perturbation peak at around $k_y = 0.06k_0$ at shorter time (solid green line in Fig. 5(b)), consistently with the previous observations. This peak decreases at later time (dotted green line) because of plasma smoothing. Three other peaks in the range of $k_y = [0.02 - 0.05]k_0$ with smaller amplitudes in Fig. 5(b) are due to mixing of ion acoustic waves travelling across the speckles. This creates density perturbations with spatial scales larger than the typical speckle waist. For $\langle I\rangle/I_{0c} = 4$ (Fig. 5(c)) and at time $t = 150$ ps, the $k_y = 0.06k_0$ peak is 5 times larger than the peak observed in the case $\langle I\rangle/I_{0c} = 1.7$. This is due to a stronger speckle self-focusing for higher laser intensity. At later time of 300 ps, the dotted grey line in Fig. 5(c) shows an almost equal distribution of density perturbations over the interval $0.01k_0 < k_y < 0.15k_0$. This broad spectrum of plasma waves is joint effect of wave steepening and mixing and beamlet divergence, as the density channels loss their initial Gaussian symmetry due to strong self-focusing (see also Fig. 4(c)) and most speckles undergo important intensity enhancement. This confirms a strong nonlinearity of the density perturbations at a high beam intensity. The beamlet divergence is studied in Sec. IV C

B. Independent speckles self-focusing: short time-scales

The dynamics of each speckle can be considered independently before plasma waves excited in different speckles interact between each other, then the individual speckle self-focusing can be studied by evaluating

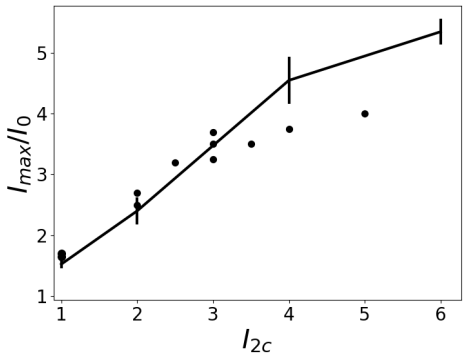

FIG. 6: Speckle intensity enhancement on short time-scales as a function of the speckle intensity normalized to three-beamlet critical intensity $I_{2c} = I_s/I_{0c}^{3b}$. The black line refers to the time-averaged intensity enhancement for a single three-beamlet case. These results are taken from our previous work[31]. The black dots stand for the intensity enhancement of several three-beamlet speckles composing the multi-speckle pattern, presented without error bars for the sake of clarity.

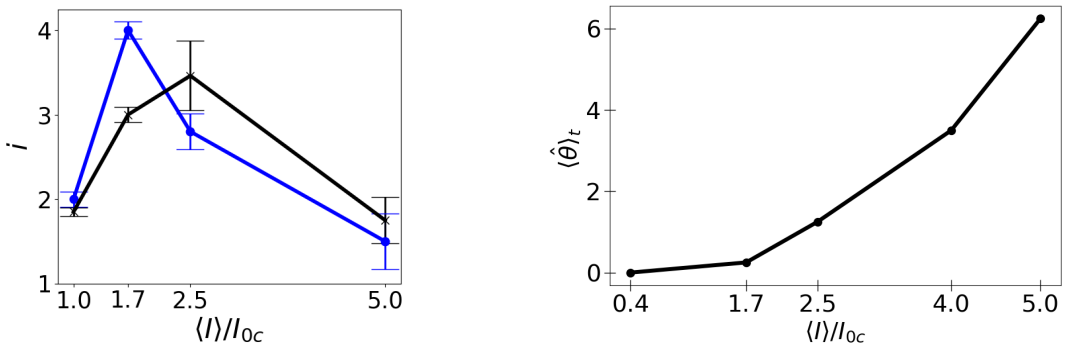

(a) (b)

FIG. 7: a) Ratio between the intensity enhancement of the most intense and less intense speckle i as a function of the beam intensity with the respective standard deviation of the mean. The blue curve refers to the intensity enhancement at $t = 150$ ps, whereas the black line to the time-average for $t > 150$ ps. b) Time-average of the beamlets average divergence $\langle\hat{\theta}\rangle_t$ as a function of the average beam intensity.

short time dynamics, i.e. for time up to $t \sim 150$ ps. At a this time-scale, one expects to retrieve the single three-beamlet speckle behavior[31]. Figure 6 shows the intensity enhancement at the stationary state of a single three-beamlet speckle presented in our previous work[31] (black line), and of several three-beamlet speckles of a multi-speckle beam (black dots) as a function of the normalized intensity $I_{2c} = I_s/I_{0c}^{3b}$, where I_{0c}^{3b} is defined by Eq. (13). The error bars refer to the standard deviation of the time-averaged mean. The black dots stand for the intensity enhancement of three-beamlet speckles composing a multi-speckle pattern averaged over a time interval of $t = [135 - 185]$ ps around $t = 150$ ps. These points are recovered from the six simulations: as the plasma conditions are similar for every case, the speckle critical intensity is equal for each speckle. Then we sample speckles from each simulation in order to represent speckles with $I_{2c} = 1, 2, 3, 4, 5$, and investigate their dynamics before inter-speckle interaction occur. The dots do not present any error bars for the sake of clarity of the graph. The figure shows that in the multi-speckle pattern the single speckle behavior at a short time is very close to the single three-beamlet speckle for speckle intensities less than four, and that this feature does not depend on a particular multi-speckle case. When the speckle intensity exceeds (4-5)I_{2c}, the intensity of all beamlets exceeds at least 4 times their own critical intensity, the beamlets strongly refract, spreading out from the speckle area and breaking the speckle symmetry. Given this refraction behind the self-focusing position, beamlets can leave the speckle and interact with beamlets in other speckles. This perturbs the single-speckle behavior and may explain why at higher speckle intensity, the intensity enhancement of a speckle in a semi-deterministic pattern is less important than the single three-beamlet speckle intensity enhancement. This stands for a limitation of the multibeamlet approach in creating the speckle pattern. However, the comparison is still satisfactory as we know that PCGO gives the best results for speckle intensity regime up to $I_{2c} = 4 - 5$ on short time scales[31].

In conclusion, the semi-deterministic method recovers our precedent results on single three-beamlet dynamics in terms of intensity enhancement when ion-acoustic waves generated by speckles self-focusing do not couple to each other, and for intensities up to 4-5 times the three-beamlet critical intensity. In the next section, we discuss the outcomes of the hydrodynamic-driven inter-speckle interaction.

C. Long time dynamics

At longer time, large amplitude plasma waves produced in high intensity speckles may interact with the less intense speckles leading to intensity amplification in the latter ones, which may be comparable to what is observed in the most intense speckles. In order to compare ponderomotive effects in the most and the less intense speckles of the speckle pattern, we calculate a ratio between the intensity enhancement of the most and less intense speckle for a given average beam intensity. This ratio is denoted by i. The dependence of this ratio on the multi-speckle beam intensity is presented in Fig. 7(a): the blue line refers to the value of time-averaged i at around $t = 150$ ps, when the hydrodynamic inter-speckle coupling has not occurred yet. The black line refers to i averaged over the rest of the simulation (150 ps $< t <$ 550 ps). The error bars stand for the standard deviation of the mean. For $\langle I\rangle/I_{0c} = 1$, a difference between the most and less intense speckle in terms of intensity enhancement is very small; this is due to the fact that the amplitude of plasma perturbation is very weak, and there is no intensity enhancement in the less intense speckles. On the contrary, a strong difference between the short time and long time behavior is observed for $\langle I\rangle/I_{0c} = 1.7$, where the most intense speckle experiences the effect of mixing

of density perturbations: a combination of linear density perturbations reduces the intensity enhancement of the most intense speckle. Consequently, the ratio i decreases over a long time. For $\langle I\rangle/I_{0c} = 2.5$ instead, we observe that the ratio i is slightly different when considering error bars of the short time (blue curve) and the long time (black curve) dynamics. In this intensity range, at short time, the intensity enhancement of the most intense speckles is saturated given that the speckle breaks due to beamlets divergence, and the less intense speckles have an initial power sufficient to develop self-focusing, although weaker than the most intense speckles. At longer times, the ratio i remains close to the short time value as evidenced by the error bars, indicating saturation of speckles self-focusing conditioned by individual beamlet behavior. When increasing the beam intensity up to $\langle I\rangle/I_{0c} = 5$, the differences in speckles intensity enhancement are minimal: this diminution is due to a combination of the speckle intensity enhancement saturation in the most intense speckle and a larger intensity enhancement in the less intense speckle. We notice that this saturation has not a physical origin, but it is due to the limitation of the ray-based method when calculating the local beamlet intensity (see Sec. II C 1). Although this is an important issue, we show in the next sections that the semi-deterministic algorithm allows to describe basic features of speckle self-focusing in a limited intensity range.

Figure 7(b) shows the time-averaged total beamlets deviation with respect to the initial straight beamlet trajectories for several cases. The angle $\langle\hat{\theta}\rangle_t$ measures the beamlets divergence, and it characterizes the beamlet spreading behind the speckle self-focusing position. The divergence increases with the average laser intensity, as speckles deviate from their initial Gaussian profile. This is particularly true for $\langle I\rangle/I_{0c} > 1$, where the average beamlet divergence above one degree is measured. This effect is due to the fact that the speckle envelope emerges from an uncorrelated sum of Gaussian beamlets intensities and highlights how high-intensity speckles undergo symmetry breaking. This fact links the saturation of the self-focusing in most intense speckles to the single beamlet behavior: the larger is the beamlets deviation, the less the speckle is Gaussian-shaped. Consequently, the speckle loses its symmetry and ponderomotive effects saturate, i.e. the intensity enhancement does not longer increase with the speckle intensity. This speckle behaviour is a feature of PCGO speckles only as the beamlets phase is neglected when evaluating PCGO beamlets' intensity overlapping. In real speckle pattern instead, beamlets interference cannot be neglected.

D. Time-integrated speckles behavior

In this section, we analyze the overall beam dynamics by considering the time-averaged speckle intensity distribution. All the cases considered are initialized with the exponential speckle statistics Eq. (7) with $f(I_s/\langle I\rangle) = \text{const}$. Ponderomotive self-focusing can substantially change the relation between the speckle abundance and their intensity, as shown in Fig. 8. In this set of figures, in log-linear scale, the dashed red lines correspond to the reference initial speckle intensity distribution, the solid blue lines refer to the speckle abundance time-averaged over all the simulation and with the relative standard deviation of the mean represented by the error bars, the dotted green lines refer to the exponential fit of the data obtained in simulations, whereas the dotted black lines refer to the fit by a power function. The solid red line in Fig. 8(a) stands for the fit of the initial statistics. Table II displays the coefficients of the linear fit of the logarithm of the data $\ln(M) = m\,(I_s/\langle I\rangle) + q$ and relative errors Δm and Δq, respectively. The log-linear plot permits to compare the slope variation of the data fit. The coefficients α and β and relative errors $\Delta\alpha$ and $\Delta\beta$ refer to the power law fit $M = \alpha\,(I_s/\langle I\rangle)^{\beta}$. The errors are calculated as a square root of the diagonal value of the covariance matrix. The row *Initial* refers to the fit of the initial exponential distribution (see red line in Fig. 3).

Figure 8(a) shows the case $\langle I\rangle/I_{0c} = 0.4$, where only the most intense speckle has an intensity comparable to the speckle critical intensity. In this case, no appreciable change of the speckle statistics is evidenced, and the intensity does not change respect to the initial distribution as reported in Table II. Given this trend, no power law fit has been performed for this case. Figure 8(b) displays the case $\langle I\rangle/I_{0c} = 1.7$, where around 20% of speckles have a intensity above the three-beamlet critical intensity. Here, self-focusing effect and plasma smoothing play an important role in the beam dynamics, but the exponential fit still holds closely to the initial shape demonstrating that the plasma-induced smoothing dominate the laser-plasma interaction. However, the high-intensity tail deviates from this behaviour, but this represents a negli-

$\langle I\rangle/I_{0c}$	m	Δm	q	Δq	α	$\Delta\alpha$	β	$\Delta\beta$
Initial	-1.1	0.1	2.4	0.2				
0.4	-1.15	0.01	2.31	0.03				
1.7	-0.89	0.07	2.21	0.03	9.5	0.4	-2.1	0.2
2.5	-0.73	0.9	2	2	7	2	-1.6	0.3
4	-0.37	0.04	1.6	0.1	5	1	-0.9	0.2

TABLE II: Coefficients for the exponential fit $M = \exp(mg + q)$ and the power fit $M = \alpha g^{\beta} + \gamma$ of the speckle probability distribution. Δa and Δb represent the uncertainties of fit parameters a and b, whereas $\Delta\alpha$ and $\Delta\beta$ are the uncertainties of fit parameters α and β. The row *Initial* refers to the linearized fit of the initial exponential distribution (see red line in Fig. 3). For all cases, $\int M(g)du = N_s$, where $g = I_s/\langle I\rangle$. The errors are calculated as a square root of the diagonal value of the covariance matrix.

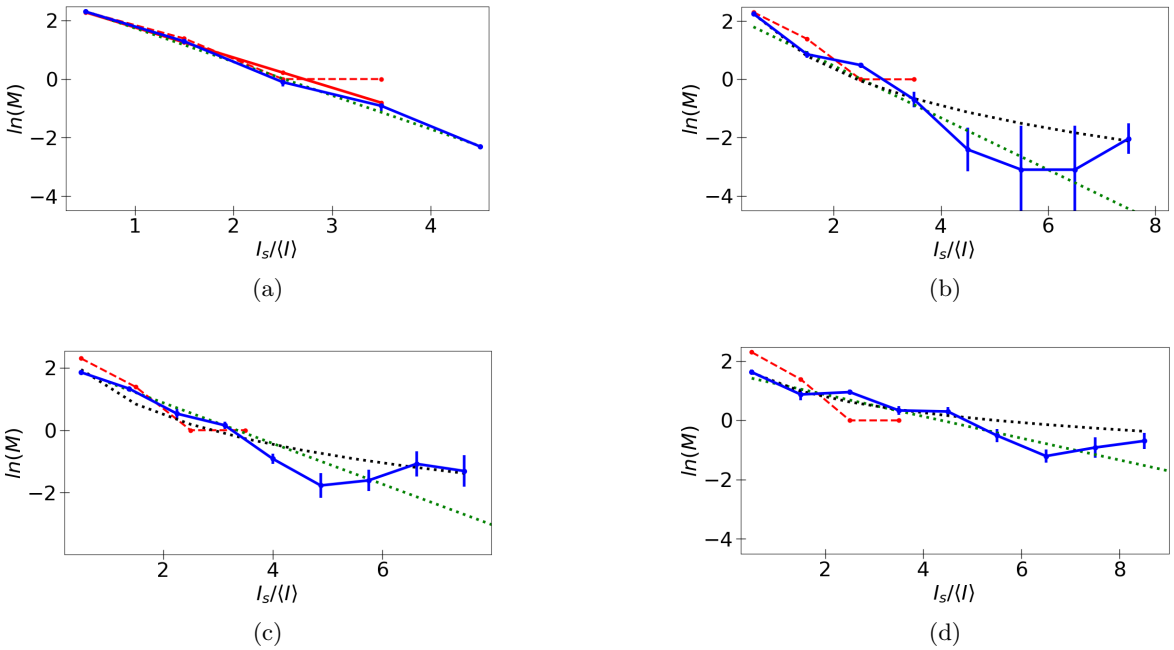

FIG. 8: Logarithm of abundance of speckles M as a function of speckle intensity normalized to the average beam intensity for a) $\langle I\rangle/I_{0c} = 0.4$, b) $\langle I\rangle/I_{0c} = 1.7$, c) $\langle I\rangle/I_{0c} = 2.5$ and d) $\langle I\rangle/I_{0c} = 4$. The dashed red lines correspond to the reference initial speckle intensity distribution, the solid blue lines refer to the time-averaged speckle abundance with the relative standard deviation of the mean represented by the error bars, the dotted green lines refer to the the exponential fit of the data obtained in simulations, whereas the dotted black lines refer to the fit by a power function. The solid red line in Fig. 8(a) stands for the fit of the initial statistics.

gible amount of the speckle intensity distribution. The abundance is modified for $\langle I\rangle/I_{0c} = 2.5$ as illustrated in Fig. 8(c), where the number of speckles having intensity above the multi-beamlet critical intensity is around 40-50%. Here, the speckle-plasma interaction and beamlets divergence play an important role. The speckle statistics is affected in both low- and high-intensity domains, but an exponential fit is preserved, even though the slope is different compared to the initial case. Here the number of high intensity speckles not following an exponential fit starts to become more relevant. The case of intensity $\langle I\rangle/I_c = 4$, where 80% of speckles have intensity above the critical intensity is shown in Fig. 8(d): here, the logarithm of data can be interpolated with a line of a slope of -0.37. The first part of the distribution can be also approximated by a power law with an exponent of -0.9. Thus the distribution does not longer preserve a pure exponential behaviour. Furthermore, the speckle abundance of the central and tail of the distribution are almost comparable. With the increasing of the laser intensity then, it is expected that the exponential distribution will be strongly modified. Therefore, the high intensity tail is enhanced and the low-intensity portion of the speckle abundance is reduced.

In order to give more indication of the approximations accuracy, we test the goodness of exponential and power law fits: we calculate the dispersion of the points evaluated by the exponential fit and by the inverse power fit compared to the data points. This is done by evaluating the reduced chi-square value for both fits:

$$\chi^2 = \frac{1}{N-s}\Sigma_j \frac{(\text{data[j]} - \text{fit[j]})^2}{\sigma^2[\text{j}]}. \qquad (16)$$

Here $j = I_s/\langle I\rangle$ represents the abscissa of the point $(I_s/\langle I\rangle, M)$, $N = 8$ is the number of bins, $s = 2$ is the number of fitting parameters, and σ are the errors measured in each bins. The index j lies in the interval [1:6]. Accurate fitting means a $\chi^2 \approx 1$, whereas $\chi^2 > 1$ and $\chi^2 < 1$ indicate poor or over fitting, respectively. Table III summarises the results for each case: the subscript exp refers to the exponential fit, whereas the subscript IP to the inverse power law function. As expected, the intensity distribution for low intensity cases show a χ^2_{exp} close to 1. By increasing the beam intensity, the exponential fit becomes less accurate, and at $\langle I\rangle/I_{0c} = 4$, both exponential and power law can approximate the results. The speckle statistics substantially changes from the initial exponential shape and a larger probability for intense speckles is observed. Plasma smoothing is no longer efficient to reduce ponderomotive effects at these intensities: high average beam intensity implies a complicate interplay between nonlinear hydrodynamics and strong speckle self-focusing leading to an important mod-

ification of the speckle intensity distribution function.

In conclusion, as a general trend, the fitting procedure demonstrates a depart from the initial statistics as the high intensity tail becomes more populated. We can identify two regimes of self-focusing of multi-speckle PCGO beams: a low and high intensity regime. The first one concerns beam intensities $\langle I\rangle/I_{0c}$ below 1.7: here the time-averaged speckle intensity statistics presents an exponential trend close to the initial speckle distribution. In this case, plasma-induced smoothing dominates and speckles do not reach a large intensity enhancement over all the time of simulation. For $\langle I\rangle/I_{0c}$ larger than 2.5, ponderomotive effects overcome the plasma smoothing: the speckle statistics shows higher intensity speckles, which is not possible to fully include in the interpolation. Given the poor statistics, it is not possible to clearly assess which fit power or exponential approximates better the results. One needs a larger number of speckles for that.

In the next section, relation between PCGO and real spatially modulated beams is assessed by comparing PCGO results to HARMONY simulations.

V. COMPARISON TO PCGO RANDOM METHOD AND ELECTROMAGNETIC SIMULATIONS

In this section, we compare the semi-deterministic method to previous works and to PCGO-CHIC runs performed with the random algorithm.

PCGO-CHIC simulations are performed by employing the random method for the plasma and laser conditions as detailed in Sec. IV for the case $\langle I\rangle/I_{0c} = 4$: the incident beam of $w_B \approx 350\lambda$ is split in 45 beamlets near the plasma boundary. These beamlets are then focused inside the plasma in a box of comparable size to the semi-deterministic case with focal position at $(500\lambda, 500\lambda)$. In this way, a pattern similar to the semi-deterministic case is created: the number of speckles is in average 12-15, with 3-4 beamlets per speckle. Also the average transverse speckle size is approximately the same as in the semi-deterministic pattern (compare Figs. 1 and 2), whereas the longitudinal average size is slightly smaller

$\langle I\rangle/I_{0c}$	$\chi^2_{\rm exp}$	$\chi^2_{\rm IP}$
0.4	0.94	-
1.7	1.35	2.05
2.5	1.8	4.2
4	0.63	1.4

TABLE III: Results of the goodness-of-fit test: the first column refers to the simulation case, the second and third columns refer to the χ^2 calculated with exponential and power fit, respectively. Here the subscript exp refers to the exponential fit, whereas the subscript IP to the inverse power law function.

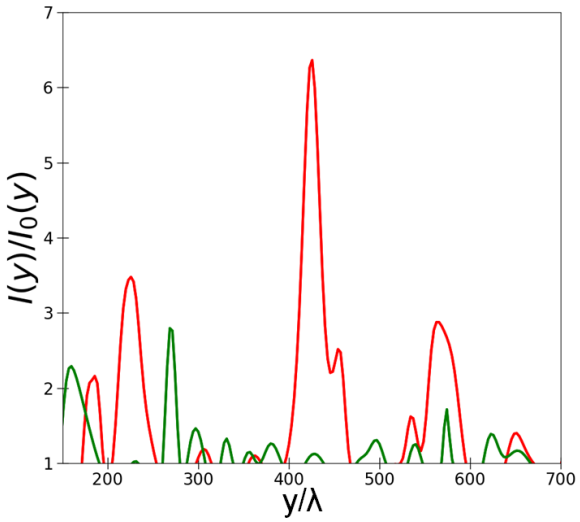

FIG. 9: Transverse line-outs of laser intensity in plasma normalized to the initial beam intensity distribution at $t = 150$ ps for simulations performed with the semi-deterministic algorithm (red line) and random algorithm (green line) showing the difference in intensity enhancement between the two cases.

as a consequence of random inclination of beamlets.

Figure 9 illustrates the transverse line-outs of the laser intensity for $t = 150$ ps and at $x = 500\lambda$ for semi-deterministic algorithm (red line) and one random algorithm run (green line). The intensity is normalized to the initial beam intensity distribution in order to easily identify the intensity amplification of the speckles: for instance, a peak value of six means an intensity amplifications of six times the initial speckle intensity located at the given position. Weaker intensity enhancements are observed in speckles built within the random method. Such a reduction is due to beamlets crossing at uncontrolled random angles and consequently, short interaction length. Furthermore, the speckle-plasma coupling arising from collective effects is inhibited because the probability of beamlets overlapping around their maximum intensities is low. Then each beamlet affects the plasma dynamics almost independently, around its peak intensity. This suppresses the collective beamlets self-focusing and arbitrarily reduces the overall speckle intensity enhancement. As we show below, the random method fails to reproduce self-focusing of realistic speckles in two-dimensional geometry.

To demonstrate this point, we compare our results against electromagnetic simulations with the code HARMONY[41] under similar plasma and laser conditions[32]. The authors performed 2D simulations to study the variation of the speckle statistics in a homogeneous plasma. HARMONY solves Eq. (1) for the electric field in the paraxial approximation, whereas the plasma is described

by the fluid equations. The code accounts for the speckle self-focusing and for near forward stimulated Brillouin scattering. The speckle size is approximately equal to the size of real speckles, that is, a few times of the laser wavelength. For the case under discussion, the number of speckles is around 2000, with an intensity abundance following the Eq. (7), and an initial speckle intensity ranging from 0.1 to 10 $\langle I \rangle$. The average beam intensity corresponds to a half of the critical intensity I_{0c}. HARMONY simulation results are presented in Fig. 10 of Ref [32], describing the time-averaged speckle abundance of the high-intensity tail $I_s/\langle I \rangle = [4, 11]$.

When comparing our simulations against HARMONY results, we need to consider the following aspects: i) PCGO does not account for the beamlets phases, and cannot describe forward Brillouin scattering. Consequently, we chose the HARMONY simulation related to the strongest ion acoustic damping, where the role of Brillouin scattering is expected to be minimal. This corresponds to the case $\langle G \rangle = 0.5$ of Fig. 10 in Ref. [32]. ii) The speckle abundance is normalized to the total number of speckles in each simulation, i.e. $N_s = 2000$ for HARMONY and $N_s = 15$ for PCGO. iii) Since PCGO and real speckles have a different critical intensity (see Eq. (13)) and ponderomotive effects depend on the relative critical intensity, it is appropriate to normalize intensity to the corresponding critical intensity, that is, $u = I_s/I_{0c}$ for HARMONY and $u = I_s/I_{0c}^{3b}$ for PCGO. iv) According to latter point, HARMONY results cover the range of $u = [2, 5]$. Given a larger speckle statistics, one PCGO realization cannot reproduce all the results. We then consider the PCGO case which most approach the HARMONY u intensity interval with a sufficient statistics. This is the case of $\langle I \rangle / I_{0c} = 2.5$, which covers the interval $u = I_s/I_{0c}^{3b} = [0.1, 5]$.

Figure 10 shows the logarithm of the speckle abundance as a function of the intensity range $u = [2, 5]$ for three cases: HARMONY $\langle I \rangle / I_{0c} = 0.5$ (blue line), PCGO semi-determinsitic method (dotted red line) and random method (dashed black line) with $\langle I \rangle / I_{0c} = 2.5$. Compared to the HARMONY results, the random algorithm (dashed black line) allows to recover the low-intensity speckle abundance but fails to follow the HARMONY trend in the high tail due to a low intensity cut-off. This is due to the fact that randomly initialized beamlet inclinations create irregular speckle intensity profile, reducing the total longitudinal speckle size. The semi-deterministic algorithm (dotted red line) instead shows an overall good agreement with the electromagnetic simulation results up to five times the PCGO speckle critical intensity. This is in agreement on what found in our previous paper for a single speckle behaviour[31].

We have demonstrated that speckle pattern built with the PCGO random algorithm exhibits too weak ponderomotive effect since beamlets are projected in the plasma box with a random inclinations, thus creating asymmetric speckles with a non-Gaussian statistics. The semi-deterministic algorithm is more appropriate for describing ponderomotive self-focusing of Gaussian-like speckles once accounted for the appropriate intensity normalization.

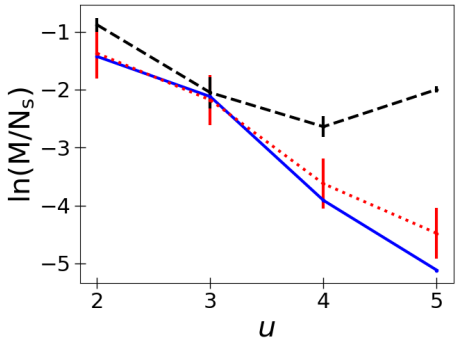

FIG. 10: Logarithm of the speckle abundance as a function of the speckle intensity bins u for three cases: HARMONY $\langle I \rangle / I_{0c} = 0.5$ (blue line), and semideterministic and random PCGO-CHIC simulations $\langle I \rangle / I_{0c} = 2.5$ (dashed red and dotted black lines, respectively). Parameter u refers to speckle intensity normalized to the related critical intensity: $u = \langle I \rangle / I_{0c}$ for HARMONY simulations, and $\langle I \rangle / I_{0c}^{3b}$ for both PCGO-CHIC simulations.. The HARMONY data are taken from S. Hüller *et al.*, New J. Physics **15**, 025003 (2013)[32].

VI. CONCLUSION

In this paper, we have improved the description of ponderomotive self-focusing effects when considering multi-speckle beams. The new PCGO-based approach, called semi-deterministic method, consists in dividing the laser beam in Gaussian-shaped speckles with a correct speckle intensity statistics. Each speckle contains three beamlets located at given positions such that to produce a Gaussian profile. This kind of speckles has a critical intensity twice larger than a 2D Gaussian beam, which accounts for the overestimation of ponderomotive effects in 2D geometry[31]. The semi-deterministic method has the following assumptions: i) it considers only one spatial degree of freedom, fixing the number of speckles and their transverse position, ii) the inter-speckle distance is the same for each speckle, and iii) the distribution of the speckle intensities is simplified by imposing $f\left(I_s/\langle I \rangle\right) = \text{const}$. The self-focusing of a semi-deterministic multi-speckle beam in a homogeneous plasma is then explored for average laser intensities ranging from $\langle I \rangle / I_{0c} = 0.4$ to 5: different regimes of plasma-speckles coupling and hydrodynamic-like inter-speckle interaction has been explored at short and long time scales.

At a short time-scale, independent speckle self-focusing is observed in agreement with results for a single three-beamlet speckle[31]: the three-beamlet speckles behave as a Gaussian beamlet having a critical intensity twice

higher than the Gaussian beam critical intensity.

At longer time-scales, density perturbations produced in neighbor speckles interfere. At moderate intensities, e.g. around $\langle I\rangle/I_{0c} = 2$, this reduces the intensity enhancement in already self-focused speckles, and it triggers self-focusing in less intense speckles. For $\langle I\rangle/I_{0c} > 2$, ponderomotive effects are saturated in the most intense speckles due to speckle symmetry breaking caused by the predominance of the individual beamlets behavior.

The analysis of time-integrated speckle abundance allows us to define two regimes of multi-speckle beam self-focusing: for a low average intensity $\langle I\rangle/I_{0c} < 2$, no appreciable changing in speckle self-focusing is induced since the amplitude of plasma perturbations remains low, i.e. of the order of 10% of the initial density, and the plasma-induced smoothing reduces the strong speckle intensity amplification. Thus the intensity statistics preserves the exponential shape. For $\langle I\rangle/I_{0c} >2$, speckle self-focusing dominates in the most intense speckles, whereas the highly nonlinear plasma perturbation triggers an intensity enhancement in less intensity speckles. As a consequence, the speckle statistics shape changes because the number of intense speckles increases and the relation between the speckle abundance and the speckle intensity fit is not clearly defined. Therefore, by increasing the beam intensity of one order of magnitude from $\langle I\rangle/I_{0c} = 0.4$ to $\langle I\rangle/I_{0c} = 5$, the speckle-plasma coupling gradually becomes nonlinear, where the intensity interval $\langle I\rangle/I_{0c} = 1.7 - 2$ represents an indicative threshold between the linear and nonlinear regime.

For intense speckles, the tail of the speckle intensity distribution strongly varies, as it has been already reported in electromagnetic simulations[32]. Our PCGO-CHIC simulations reproduce the modification of the speckle distribution tail observed in two-dimensional electromagnetic simulations once accounted for electromagnetic and PCGO speckle differences and when using the present semi-deterministic approach over the random method. Thus, our results demonstrate that shaping Gaussian speckle by overlapping three beamlets and imposing the correct speckle intensity abundance allow to describe ponderomotive self-focusing in the ray-based PCGO framework. These results agree with single three-beamlet speckle simulations[31], where we have found that the PCGO method can be applied to speckles with an intensity up to 4-5 times larger than the critical intensity.

In future work, immediate improvements based on this method should account for i) extending the semi-deterministic approach to more general conditions found in spatially modulated beams, e.g. random inter-speckle distance and/or different statistics, ii) including other properties of spatially modulated beams such as beam contrast, and iii) implementing a temporal variation of speckle positions at the end of a certain time interval to mimic temporal smoothing.

ACKNOWLEDGMENTS

This work has been carried out within the framework of the EUROfusion Consortium and has received funding from the Euratom research and training program 2014-2018 and 2019-2020 under grant agreement No 633053. The views and opinions expressed herein do not necessarily reflect those of the European Commission. The authors acknowledge A. Colaïtis for his suggestions on the CHIC code, and S. Hüller, A. Debayle, R. H. H. Scott and C. Riconda for useful discussions. The authors are grateful to the reviewers, whose suggestions allowed to highly improve the manuscript. This research was partially supported by the Project LQ1606 with the financial support of the Ministry of Education, Youth and Sports as part of targeted support from the Czech National Program of Sustainability II.

[1] J. D. Lindl, "*Inertial Confinement Fusion: The Quest for Ignition and Energy Gain Using Indirect Drive*", AIP-Press (1998).
[2] S. Atzeni, J. Meyer-ter-Vehn, "The Physics of Inertial Fusion", Oxford University Press Canada, (2009).
[3] R. Betti, C. D. Zhou, K. S. Anderson, L. J. Perkins, W. Theobald, and A. A. Solodov, "*Shock Ignition of Thermonuclear Fuel with High Areal Density*", Phys. Rev. Lett. 98, 155001 (2017). doi: 10.1103/PhysRevLett.98.155001.
[4] S. Atzeni, A. Marocchino and A. Schiavi, "*Shock ignition: a brief overview and progress in the design of robust targets*", Plasma Phys. and Controlled Fusion, **57** 014022 (2015). doi: 10.1063/1.5003814.
[5] V T Tikhonchuk, A Colaïtis, A Vallet, E Llor Aisa, G Duchateau, Ph Nicolaï and X Ribeyre, "*Physics of laser-plasma interaction for shock ignition of fusion reactions*", Plasma Phys. and Controlled Fusion, **58** 014018 (2015). doi:10.1088/0741-3335/58/1/014018.
[6] S. Atzeni, J.R. Davies, L. Hallo, J.J. Honrubia, P.H. Maire, M. Olazabal-Loumé, J.L. Feugeas, X. Ribeyre, A. Schiavi, G. Schurtz, J. Breil and Ph. Nicolaï, "*Studies on targets for inertial fusion ignition demonstration at the HiPER facility*", Nuclear Fusion, **49**, Number 5055008 (2009). doi:10.1088/0029-5515/49/5/055008.
[7] T. R. Boehly, D. Munro, P. M. Celliers, R. E. Olson, D. G. Hicks, V. N. Goncharov, G. W. Collins, H. F. Robey, S. X. Hu, J. A. Morozas, T. C. Sangster, O. L. Landen, and D. D. Meyerhofer, "*Demonstration of the shock-timing technique for ignition targets on the National Ignition Facility*", Phys. Plasmas 16, 056302 (2009). doi:10.1063/1.3078422.
[8] S. Guskov, X. Ribeyre, M. Touati, J.L. Feugeas, P. Nicolaï, V. Tikhonchuk, "*Ablation pressure driven by an energetic electron beam in a dense plasma*", Phys Rev Lett. **109** 255004(2012). doi:10.1103/PhysRevLett.109.255004.
[9] E Aisa, X. Ribeyre, G. Duchateau, T. Nguyen-Bui, V. Tikhonchuk, A.Colaïtis, R. Betti, A. Bose, W. Theobald, "*The role of hot electrons in the dynamics of a laser-driven strong converging shock*", Phys. Plasmas **24**, 112711 (2017). doi: 10.1063/1.5003814.
[10] W. Theobald, A. Bose, R. Yan, R. Betti, M. Lafon, D. Mangino, A. R. Christopherson, C. Stoeckl, W. Seka, W. Shang), D. T. Michel, C. Ren, R. C. Nora, A. Casner, J. Peebles, F. N. Beg, X. Ribeyre, E. Llor Aisa, A. Colaïtis, V. Tikhonchuk, M. S. Wei, "*Enhanced hot-electron production and strong-shock generation in hydrogen-rich ablators for shock ignition* ", Phys. Plasmas **24**, 120702 (2017). doi:10.1063/1.4986797.
[11] Y. Kato, K. Mima, *N*. Miyanaga, S. Arinaga, Y. Kitagawa, M. Nakatsuka, and C. Yamanaka, "*Random Phasing of High-Power Lasers for Uniform Target Acceleration and Plasma-*

Instability Suppression", Phys. Rev. Lett. **53**, 1057 (1984). doi: 10.1103/PhysRevLett.53.1057.

[12]S. N. Dixit, J. K. Lawson, K. R. Manes, H. T. Powell, and K. A. Nugent, "*Kinoform phase plates for focal plane irradiance profile control*", Optics Letters **19**, Issue 6, pp. 417-419 (1994). doi:10.1364/OL.19.000417.

[13]J. Neauport, X. Ribeyre, J. Daurios, D. Valla, M. Lavergne, V. Beau, and L. Videau, "*Design and optical characterization of a large continuous phase plate for Laser Integration Line and laser Megajoule facilities*", *Appl. Opt.* **42**, 13, (1997). doi: 10.1364/AO.42.002377.

[14]H. Rose, D. F. Dubois, "*Statistical properties of laser hot spots produced by a random phase plate*", Phys. Fluids B**5**, 590 (1993). doi:10.1063/1.860545.

[15]J. Garnier, "*Statistics of the hot spots of smoothed beams produced by random phase plates revisited*", Phys. Plasmas **6**, 1601 (1999). doi:10.1063/1.873413.

[16]E. A. Williams, "*On the control of filamentation of intense laser beams propagating in underdense plasma*, Phys. Plasmas **13**, 056310 (2006). doi:10.1063/1.2179051.

[17]C. J. Randall, J. R. Albritton, and J. J. Thomson, "*Theory and simulation of stimulated Brillouin scatter excited by nonabsorbed light in laser fusion systems*", Phys. Fluids **24**, 1474 (1981). doi:10.1063/1.863551.

[18]S. Hüller, G. Raj, W. Rozmus, and D. Pesme, "*Crossed beam energy transfer in the presence of laser speckle ponderomotive self-focusing and nonlinear sound waves*", Phys. Plasmas **27**, 022703 (2020). doi:10.1063/1.5125759.

[19]D. Batani, S. Baton, A. Casner, S. Depierreux, M. Hohenberger, O. Klimo, M. Koenig, C. Labaune, X. Ribeyre, C. Rousseaux, G. Schurtz, W. Theobald and V.T. Tikhonchuk, "*Physics issues for shock ignition*" Nucl. Fusion **54**, 054009 (2014). doi: 10.1088/0029-5515/54/5/054009.

[20]T.B. Kaiser, "*Laser ray tracing and power deposition on an unstructured three-dimensional grid*", Phys. Rev. E, **89**, 1 (2000). doi:10.1103/PhysRevE.61.895.

[21]A Jaun, E R Tracy and A N Kaufman, "*Eikonal waves, caustics and mode conversion in tokamak plasmas*", Phys. Rev. E, **89**, 1 (2000). doi:10.1088/0741-3335/49/1/004.

[22]K. Yanagihara, I. Y. Dodin, and S. Kubo, "*Quasioptical modeling of wave beams with and without mode conversion. II. Numerical simulations of single-mode beams*", Plasma Phys. Control. Fusion **49**, 43 (2007). doi:10.1063/1.5095173.

[23]A A Balakin, M A Balakina, G V Permitin and A I Smirnov, "*Quasi-optical description of wave beams in smoothly inhomogeneous anisotropic media*", J. Phys. D: Appl. Phys. **40** 4285 (2007). doi:10.1088/0022-3727/40/14/028.

[24]R.A. Cairns and V. Fuchs, "*Calculation of a wave field from ray tracing*", Nucl. Fusion **50** 095001 (10pp) (2010). doi: 10.1088/0029-5515/50/9/095001.

[25]A. Debayle, C. Ruyer, O. Morice, P.-E. Masson-Laborde, P. Loiseau, and D. Benisti, "*A unified modeling of wave mixing processes with the ray tracing method*", Phys. Plasmas **26** 092705 (2019); doi:10.1063/1.5110247.

[26]I. V. Igumenshchev, D. H. Edgell, V. N. Goncharov, J. A. Delettrez, A. V. Maximov, J. F. Myatt, W. Seka, A. Shvydky, S. Skupsky, and C. Stoeckl, "*Crossed-beam energy transfer in implosion experiments on OMEGA*", Phys. Plasmas **17** 122708 (2010); doi: 10.1063/1.3532817.

[27]A. Colaïtis, G. Duchateau, Ph. Nicolaï and V. Tikhonchuk, "*Towards modeling of nonlinear laser-plasma interactions with hydrocodes: The thick-ray approach*" Phys. Rev. E **89**, 033101 (2014). doi:10.1103/PhysRevE.89.033101.

[28]J. Breil, S. Galera and P.H. Maire, "*Multi-material ALE computation in inertial confinement fusion code CHIC*", Computers Fluids **46**, 161 (2011). doi:10.1016/J.COMPFLUID.2010.06.017.

[29]Y. A. Kravtsov, Y. I Orlov, "Geometrical Optics of Inhomogeneous Media", Springer-Verlag, (1990).

[30]A. Colaïtis,, "Multi-scale description of the laser-plasma interaction: application to the physics of shock ignition in inertial confinement fusion", PhD thesis, University of Bordeaux (2016).

[31]A. Ruocco, G. Duchateau, V. T. Tikhonchuk, and S. Hüller, "*Modeling of laser ponderomotive self-focusing in plasma within the paraxial complex geometrical optics approach*", Plasma Phys. Control. Fusion **61**, 115009 (2019). doi:10.1088/1361-6587/ab467b.

[32]S. Hüller, A. Porzio and J. Robiche, *Order statistics of high-intensity speckles in stimulated Brillouin scattering and plasma-induced laser beam smoothing*, New J. Physics **15**, 025003 (2013). doi:10.1088/1367-2630/15/2/025003.

[33]W. Kruer, "The Physics Of Laser Plasma Interactions", CRC Press (2003).

[34]C.E. Max, "*Strong self-focusing due to the ponderomotive force in plasmas*", Phys. Fluids **19**, 74 (1976). doi:10.1063/1.861305.

[35]H. A. Rose and D. F. DuBois, "*Initial development of ponderomotive filaments in plasma from intense hot spots produced by a random phase plate*", Phys. Fluids B **5**, 3337 (1993). doi: 10.1063/1.860629.

[36]V. Tikhonchuk, S. Hüller, P. Mounaix, "*Effect of the speckle self-focusing on the stationary stimulated Brillouin scattering reflectivity from a randomized laser beam in an inhomogeneous plasma*", Phys. Plasmas **4**, 4369 (1997). doi:10.1063/1.872599.

[37]A. V. Maximov, I. G. Ourdev, D. Pesme, W. Rozmus, V. T. Tikhonchuk, and C. E. Capjack, "*Plasma induced smoothing of a spatially incoherent laser beam and reduction of backward stimulated Brillouin scattering*", Phys. Plasmas **8**, 1319 (2001). doi: 10.1063/1.1352056.

[38]C. Labaune, S. Baton, T. Jalinaud, H. A. Baldis, and D. Pesme, "*Filamentation in long scale lengthplasmas: Experimental evidence andeffects of laser spatial incoherence*", Phys. Fluids B **4**, 2224 (1992). doi:10.1063/1.860027.

[39]A. Schmitt and B. Afeyan, "*Time-dependent filamentation and stimulated Brillouin forward scattering in inertialconfinement fusion plasma*", Phys. of Plasmas **5**, 503 (1998). doi: 10.1063/1.872733.

[40]A. Colaïtis, G. Duchateau, X. Ribeyre and V. Tikhonchuk, "*Modeling of the cross-beam energy transfer with realistic inertial-confinement-fusion beams in a large-scale hydrocode*" Phys. Rev. E **91**, 013102 (2015). doi:10.1103/PhysRevE.89.033101.

[41]S. Hüller, P. E. Masson-Laborde, D. Pesme, M. Casanova, F. Detering and A. Maximov, "*Harmonic decomposition to describe the nonlinear evolution of stimulated Brillouin scattering*", Phys. Plasmas **13**, 022703 (2006). doi:10.1063/1.2168403.